

Flexible Conductive Polyimide Fiber/MXene Composite Film for Electromagnetic Interference Shielding and Joule Heating with Excellent Harsh Environment Tolerance

Kang Sun, Fan Wang, Wenke Yang, Hu Liu,* Caofeng Pan, Zhanhu Guo, Chuntai Liu, and Changyu Shen

Cite This: *ACS Appl. Mater. Interfaces* 2021, 13, 50368–50380

Read Online

ACCESS |

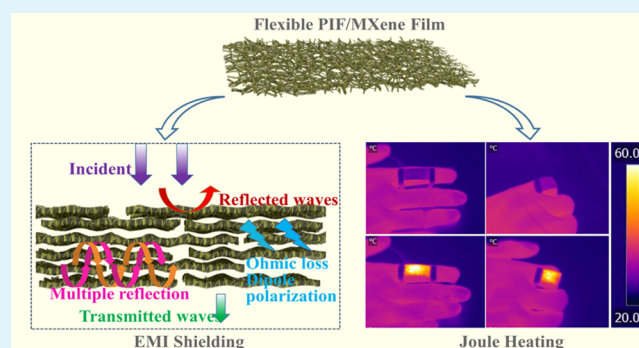
Metrics & More

Article Recommendations

Supporting Information

ABSTRACT: The development of flexible MXene-based multi-functional composites is becoming a hot research area to achieve the application of conductive MXene in wearable electric instruments. Herein, a flexible conductive polyimide fiber (PIF)/MXene composite film with densely stacked “rebar-brick-cement” lamellar structure is fabricated using the simple vacuum filtration plus thermal imidization technique. A water-soluble polyimide precursor, poly(amic acid), is applied to act as a binder and dispersant to ensure the homogeneous dispersion of MXene and its good interfacial adhesion with PIF after thermal imidization, resulting in excellent mechanical robustness and high conductivity (3787.9 S/m). Owing to the reflection on the surface, absorption through conduction loss and interfacial/dipolar polarization loss inside the material, and the lamellar structure that is beneficial for multiple reflection and scattering between adjacent layers, the resultant PIF/MXene composite film exhibits a high electromagnetic interference (EMI) shielding effectiveness of 49.9 dB in the frequency range of 8.2–12.4 GHz. More importantly, its EMI shielding capacity can be well maintained in various harsh environments (e.g., extreme high/low temperature, acid/salt solution, and long-term cyclic bending), showing excellent stability and durability. Furthermore, it also presents fast, stable, and long-term durable Joule heating performances based on its stable and excellent conductivity, demonstrating good thermal deicing effects under actual conditions. Therefore, we believe that the flexible conductive PIF/MXene composite film with excellent conductivity and harsh environment tolerance possesses promising potential for electromagnetic wave protection and personal thermal management.

KEYWORDS: polyimide fiber, MXene, lamellar structure, EMI shielding, Joule heating



1. INTRODUCTION

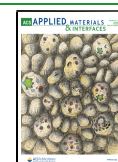
With the advent of the information age, lots of electronic devices that use high-frequency and high-power electromagnetic waves (EMWs) for interconnection have been widely used. However, the generated electromagnetic radiation or interference would threaten the operation reliability of precise instruments and human health seriously, promoting the rapid research and development of highly efficient electromagnetic interference (EMI) shielding materials.^{1–4} Traditionally, metal and metallic alloys are chosen as the EMI shielding materials with favorable EMI shielding effectiveness (SE) higher than 60 dB based on their high electrical conductivity and shallow skin depth, but their high weight density, poor flexibility, and poor chemical corrosion resistance limit their wide applications to some extent.^{5,6} Herein, some efforts have been devoted to seeking promising substitutes with high EMI SE, lightweight, and good flexibility.^{7–9}

Conductive polymer composites (CPCs) with the merits of good flexibility, excellent conductivity, and easy processing have been approved to be the most promising EMI shielding materials. Generally, CPCs are obtained by combining the insulated polymer [e.g., poly(vinylidene fluoride),¹⁰ cellulose nanofiber,¹¹ and nitrile butadiene rubber (NBR)³ and conductive filler (e.g., carbon black,¹² carbon nanotubes,⁴⁵ graphene,^{13,14,46} silver nanofiber,^{15,16} and MXene^{17–22}) together through a proper processing technology. More importantly, electrical conductivity, which is the key factor determining the EMI SE of a material, could be effectively tuned through

Received: August 13, 2021

Accepted: October 6, 2021

Published: October 15, 2021



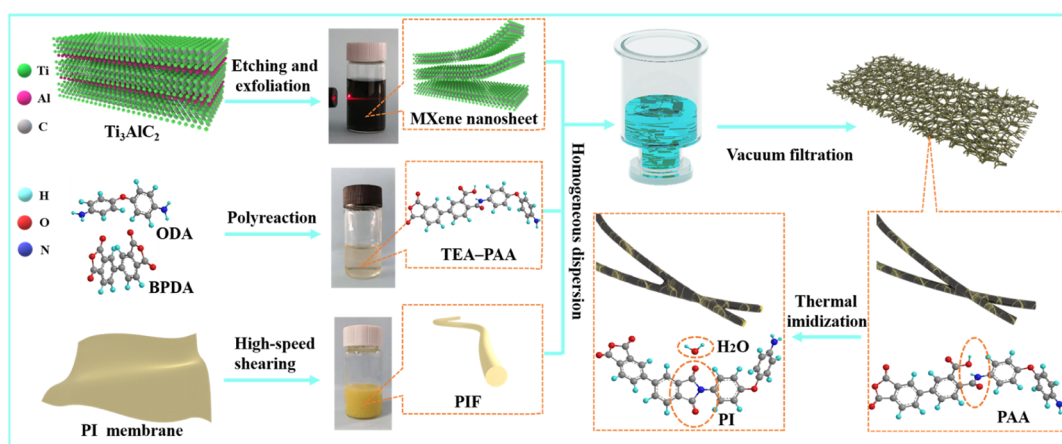


Figure 1. Schematic illustration for the fabrication of flexible conductive PIF/MXene composite films.

changing the conductive filler loading of CPCs, satisfying different shielding requirements. For example, Das's group conducted a series of related studies,^{23–26} and the EMI SE of the reported wool/nylon polymer nanocomposites increases from 8.65 to 73.8 dB at 1–20 dipping cycles, which affects the coated PEDOT:PSS/reduced graphene oxide loading directly.²³ Besides, CPCs with special structures, including porous structure,²⁷ segregated structure,²⁸ alternating multilayer structure,^{29,30} and nacre-like structure,¹¹ can also be designed easily to further enhance their EMI shielding performance based on the multiple reflections of EMWs.

Recently, $\text{Ti}_3\text{C}_2\text{T}_x$ MXene, as one of the newly emerged two-dimensional transition-metal carbides and/or nitrides, has attracted tremendous attention for EMI shielding applications based on its excellent metallic conductivity and multiple layer structures. For example, a pure $\text{Ti}_3\text{C}_2\text{T}_x$ film with an EMI SE up to 93 dB at a thickness of 40 μm was acquired due to its ultrahigh conductivity of $5225 \text{ S}\cdot\text{cm}^{-1}$ and multiple internal reflections.³¹ However, the pure $\text{Ti}_3\text{C}_2\text{T}_x$ film usually presents poor mechanical properties, and the Ti atom also has poor oxidation resistance in humid air or water,³² affecting its practical application badly. In this case, the preparation of flexible MXene-based CPCs turns to be an effective route to solve the above problems. Meanwhile, the abundant active polar functional groups (e.g., $-\text{O}$, $-\text{F}$, and $-\text{OH}$) on the surface of MXene also facilitate the formation of hydrogen bonding with the polymer matrix,^{22,33–35} including sodium alginate,² cellulose nanofibers,¹¹ NBR,³ and polystyrene,²² endowing the CPCs with improved robustness. However, the poor harsh environment (e.g., extreme temperature, water, and acid–base solution) tolerance of those conventional polymers can undoubtedly restrict their stability of EMI shielding performances.

In this work, polyimide fiber (PIF), which possesses high-/low-temperature resistance, high mechanical strength, chemical and radiation resistance, and good flexibility,^{36–39} was chosen as the polymeric matrix for the preparation of flexible conductive PIF/MXene composite films through the vacuum filtration plus thermal imidization technique. Here, the water-soluble polyimide (PI) precursor, poly(amic acid) (PAA), was applied to act as a binder and dispersant to ensure the homogeneous dispersion of MXene and its good adhesion with PIF, constructing the densely stacked “rebar-brick-cement” (PIF-PAA-MXene) lamellar structure. After the transformation of PAA into PI during the thermal imidization process, robust PIF/MXene composite films were successfully prepared. The

microstructure, mechanical properties, electrical conductivity, and EMI shielding performances as a function of MXene loading were investigated in detail. Especially, the prepared flexible conductive PIF/MXene composite film exhibits stable EMI shielding performances toward different harsh environments, such as extreme high/low temperature, acid/salt solution, and repeated bending, showing excellent harsh environment tolerance when served as EMI shielding materials. Moreover, the flexible conductive composite film also presents fast, stable, and long-term durable Joule heating performances based on its stable and excellent conductivity. Therefore, our prepared flexible conductive PIF/MXene composite film possesses great industrialization potential in advanced wearable EMI shielding and thermal management applications.

2. EXPERIMENTAL SECTION

2.1. Materials and Chemicals. Titanium aluminum carbide (Ti_3AlC_2 , 400 mesh) was purchased from Jilin 11 Technology Co., Ltd (China). Lithium fluoride (LiF), 4,4'-diaminodiphenyl ether (ODA, 98%), and 3,3',4,4'-biphenyltetracarboxylic dianhydride (BPDA, 97%) were obtained from Shanghai Aladdin Biochemical Technology Co., Ltd (China). Hydrochloric acid (HCl) was provided by Luoyang Haohua Chemical Reagent Co., Ltd (China). *N*-Methyl-2-pyrrolidone (NMP, AR) was bought from Tianjin Kermel Chemical Reagent Co., Ltd (China). Triethylamine (TEA, AR) was supplied by Tianjin Damao Chemical Reagent Factory (China). PIF (fiber diameter $\approx 400 \text{ nm}$) membranes were bought from Jiangxi Xiancai Nanofibers Technology Co., Ltd (China). All the chemicals and materials were used as received, except that BPDA was vacuum dried at 80 $^\circ\text{C}$ for 10 h before use.

2.2. Preparation of $\text{Ti}_3\text{C}_2\text{T}_x$ MXene Nanosheets. According to our previous studies,^{33,40–43} a high-quality $\text{Ti}_3\text{C}_2\text{T}_x$ MXene nanosheet was prepared by selectively etching the Al atomic layer from the Ti_3AlC_2 MAX phase. Typically, 2 g of LiF was first dissolved in 40 mL of HCl at room temperature (25 $^\circ\text{C}$), and 2 g of Ti_3AlC_2 powder was then slowly added and stirred in an oil bath (35 $^\circ\text{C}$) for 24 h to completely etch the Al atomic layer. Subsequently, aiming to remove the residual LiF, HCl, and other impurities, the obtained suspension was separated by centrifugation (3500 rpm, 10 min) and washed with deionized (DI) water under shaking alternately 4–5 times until the pH value of the supernatant was higher than 5. Thereafter, the obtained black centrifugal sedimentation was redispersed with 40 mL of ethanol, ultrasonically treated (200 W, 60 min), and separated by centrifugation (10 000 rpm, 10 min) successively, achieving black exfoliated MXene nanosheets. Finally, the exfoliated products were dispersed in DI water and centrifuged (3500 rpm, 3 min) several times to collect the upper dark green supernatant. As a result, a few-layer $\text{Ti}_3\text{C}_2\text{T}_x$ MXene nanosheet suspension with a concentration of 5 mg/mL was acquired.

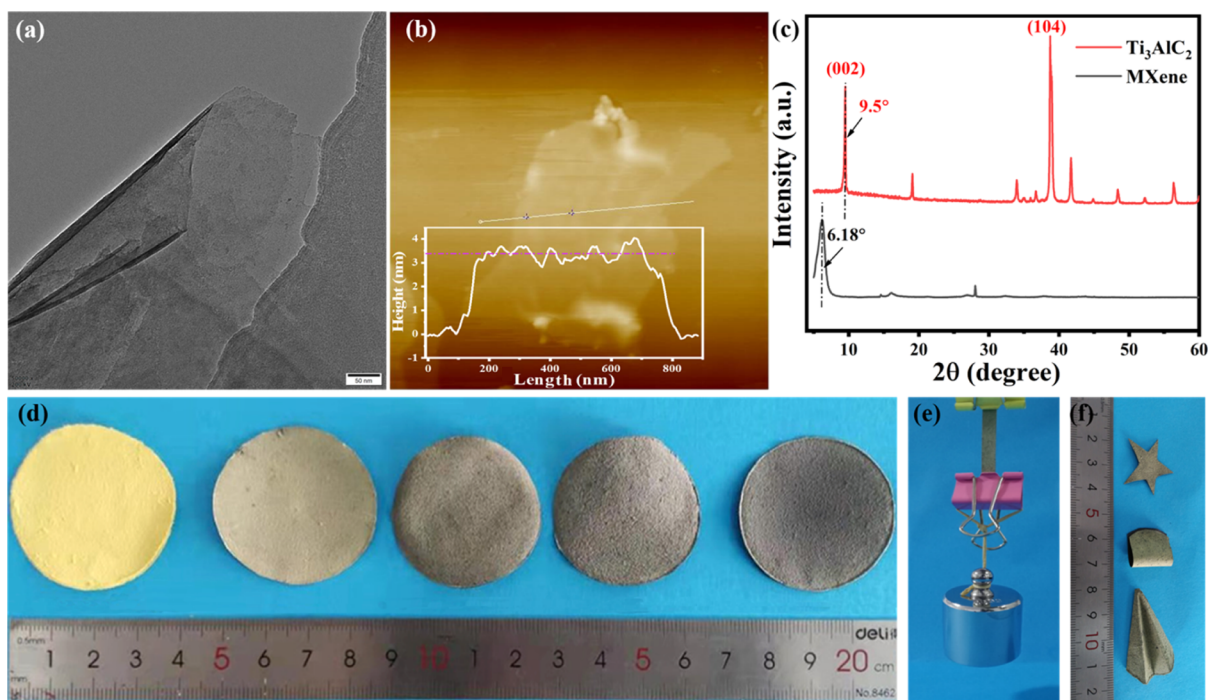


Figure 2. (a) TEM and (b) AFM images of MXene nanosheets. (c) XRD patterns of Ti_3AlC_2 and MXene. (d) Digital pictures of the pure PIF film and different PIF/MXene composite films. Digital pictures showing (e) excellent tailorability, bendability, foldability and (f) good tensile strength of the prepared PIF/MXene composite film.

2.3. Preparation of Water-Soluble PAA. Water-soluble PAA was synthesized according to the previously reported polycondensation procedure, Figure S1.^{40,44} Typically, ODA (4.00 g, 0.02 mol) and BPDA (5.88 g, 0.02 mol) were dissolved in 60 mL of NMP successively under mechanical stirring in an ice–water bath for 10 h. After that, TEA (2.78 mL 0.02 mol) was added and stirred for another 2 h to obtain a light yellow viscous solution, which was then slowly poured into 1000 mL of DI water at 0 °C, generating the white water-soluble TEA-capped PAA precipitate. After filtering and washing with DI water, the PAA precipitate was freeze-dried (10 Pa, –80 °C) for 48 h and grinded for further use.

2.4. Preparation of Flexible Conductive PIF/MXene Composite Films. Figure 1 illustrates the procedure for fabricating the flexible conductive PIF/MXene composite film. In brief, 200 mg of the PIF membrane was first shredded into small pieces with a dimension of $3 \times 3 \text{ mm}^2$ and soaked in 40 mL of dioxane for 15 h, which was then treated using a high-shearing homogenizer (FJ200-SH) at a speed of 13,000 rpm for 30 min, and fluffy PIF (Figure S2) was acquired after freeze-drying (10 Pa, –80 °C) for 48 h. Subsequently, homogeneous yellow PIF aqueous suspension was prepared by adding 50 mg of PIF and 30 mg of PAA into 10 mL of 5 vol % TEA aqueous solution under stirring for 1 h, followed by adding 12.5 mg of MXene nanosheet under mechanical stirring for 20 min. Finally, the homogeneous black PIF/MXene mixture was treated using the simple vacuum filtration technique, and the obtained filler cake was dried in an oven at 50 °C for 30 min and further thermal imidized (100 °C, 1 h; 200 °C, 1 h; and 300 °C, 1 h) at a heating rate of 5 °C/min under a nitrogen atmosphere, resulting in the designed flexible conductive PIF/MXene composite film. In this work, a series of PIF/MXene composite films were prepared by adjusting the MXene loading, and the PIF/MXene composite films with 12.5 mg (13.8 wt %), 25 mg (24.3 wt %), 50 mg (39.1 wt %), and 75 mg (49.1 wt %) MXene were denoted as PM-13.8, PM-24.3, PM-39.1, and PM-49.1, respectively. In addition, a pure PIF film without the addition of MXene nanosheets was also prepared using the same procedure.

2.5. Characterizations. Morphology and size of MXene nanosheets were observed using a transmission electron microscope (JEOL JEM-2100F) and an atomic force microscope (MFP-3D Origin+/icon).

Scanning electron microscopy (SEM) was conducted on a JEOL JSM-7500F instrument at an accelerating voltage of 5 kV. Raman spectra were recorded using a Raman spectrometer (HORIBA Lab RAM HR Evolution) with a laser excitation of 488 nm and a resolution of 1 cm^{-1} . Fourier transform infrared (FTIR) spectra in the range of 400 to 4000 cm^{-1} were recorded on a Nicolet Nexus 870 instrument using the attenuated total reflection mode. X-ray photoelectron spectroscopy (XPS) was measured using an X-ray photoelectron spectrometer (Thermo ESCALAB 250XI) with an excitation source of Al $K\alpha$ radiation. The tensile mechanical property test is operated on an electronic universal testing machine (UTM2203, load cell = 100 N, Shenzhen Suns Technology Stock Co. Ltd., China). The electrical property was measured using a 4-point Probes resistivity meter (RTS-8). The Joule heating performance was characterized by charging a certain voltage supplied by a DC power supply (UTP 1306S, UNI-T) and then in situ monitoring the temperature change using the infrared thermal imaging camera (E60, FLIR). The EMI shielding performance test was conducted using a network analyzer (Agilent Technologies N5244A) with the wave-guide method. Based on the recorded scattering parameters (S_{11} and S_{21}) in the frequency range of 8.2–12.4 GHz (X-band), transmission coefficient (T), reflection coefficient (R), absorption coefficient (A), total SE (SE_T) and its components of (SE_R), and absorption (SE_A) were calculated using the following equations.

$$R = |S_{11}|^2$$

$$T = |S_{21}|^2$$

$$A = 1 - R - T$$

$$\text{SE}_R = -10 \log(1 - R)$$

$$\text{SE}_A = -10 \log \frac{T}{1 - R}$$

$$\text{SE}_T = \text{SE}_R + \text{SE}_A + \text{SE}_M$$

where the multiple internal reflections (SE_M) can be negligible when SE_T is higher than 10 dB.⁴⁵

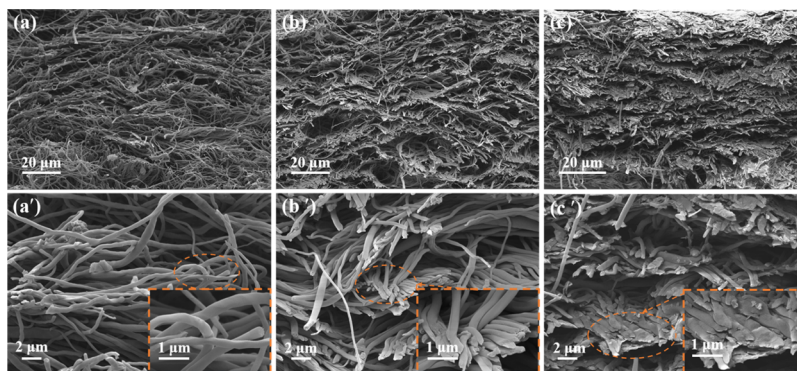


Figure 3. Cross-sectional SEM images of the pure PIF film (a,a') before and (b,b') after thermal imidization treatment and (c,c') PM-13.8 under different magnifications.

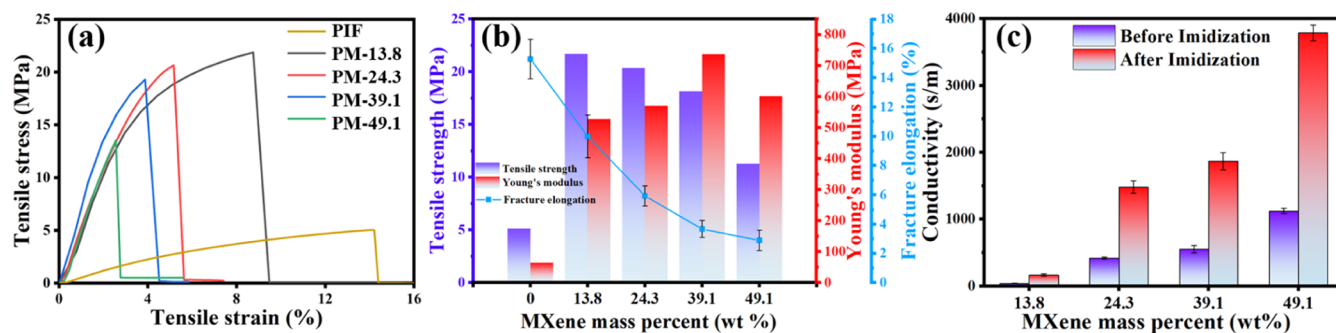


Figure 4. (a) Typical stress–strain curves and (b) corresponding mechanical properties of PIF/MXene composite films with different MXene loadings. (c) Electrical conductivity of PIF/MXene composite films with different MXene loadings before and after thermal imidization treatment.

3. RESULTS AND DISCUSSION

3.1. Fabrication of PIF/MXene Composite Films.

Flexible conductive PIF/MXene composite films were prepared through the vacuum filtration plus thermal imidization technique, and the details are listed in the experimental part. First, MXene nanosheet is prepared through the etching and deamination technique, and the transmission electron microscopy (TEM) (Figure 2a) and atomic force microscopy (AFM) (Figure 2b) images prove that the transparent and flexible MXene nanosheet with an average lateral size of 600 nm and a thickness of 3.4 nm were successfully obtained. As a result, the final MXene aqueous dispersion displays the typical “Tyndall effect” due to the nanometer dimension and amounts of hydrophilic groups of MXene nanosheet. In addition, the successful preparation of MXene nanosheet is also verified from the XRD results (Figure 2c). Comparing with Ti_3AlC_2 , the strong (104) peak vanishes completely for MXene, which is mainly due to the successful etching of the Al atomic layer. In addition, the (002) peak shifts from 9.5° to 6.18° , indicating that the interlayer spacing increases from 4.67 to 7.16 nm, which is strong evidence for the extension of the interlayer distance arising from the successful delamination of the layered Ti_3AlC_2 . More importantly, the sharpness of the (002) peak confirms that the crystallinity and structure of Ti_3AlC_2 are well retained during the preparation process. After that, a series of PIF/MXene composite films were prepared by mixing MXene aqueous dispersion with PIF (average length: $\sim 50 \mu\text{m}$, Figure S3) suspension and PAA solution at a certain mass ratio, which was then vacuum-filtered, dried, and processed by thermal imidization sequentially. As can be seen in Figure 2d, the color of the fabricated PIF/MXene composite film gradually changes from the yellow of the pure PIF film to black with

increasing MXene nanosheet loading, and the rough surface of the pure PIF film is also well kept. Here, it should be noted that PAA can be completely converted into PI during the thermal imidization process (Figure S1), enabling it to act as a binder to ensure the strong PIF–PIF and PIF–MXene interfacial adhesion. As a result, the obtained PIF/MXene composite film can bear a 200 g weight (about 13,600 times its weight) without being destroyed (Figure 2e), exhibiting excellent tensile mechanical property. Besides, based on the good flexibility of PIF, the PIF/MXene composite film exhibits excellent tailorability, bendability, and foldability (Figure 2f), which can effectively solve the disadvantage of brittleness of the pure MXene film (Figure S4), promoting the wide application of MXene in the field of flexible electronics.

3.2. Morphology, Mechanical Property, and Conductivity Analysis. To verify the interfacial adhesion role of PAA, the cross-sectional SEM images of the pure PIF film before and after thermal imidization treatment and PM-13.8 were systematically investigated, Figure 3. Clearly, special hierarchical lamellar structure is well observed for all samples due to the vacuum-assisted self-assembly process, but the pure PIF film before thermal imidization treatment is less obvious due to the loosely physically entangled PIF (Figure 3a,a'). After the thermal imidization treatment process, the pure PIF film presents a denser and obvious aligned lamellar cross-section, where PIF are strongly welded together with the help of thermal-imidized PI (Figure 3b,b'). As for the PIF/MXene composite film, tightly stacked lamellar structure without an obvious interlayer gap is obtained especially for the composite film with higher MXene loading (Figure 3c,c' and S5), where PIF serves as a “rebar” to construct the main skeleton of the composite film, MXene nanosheets serve as “brick” to further reinforce the PIF

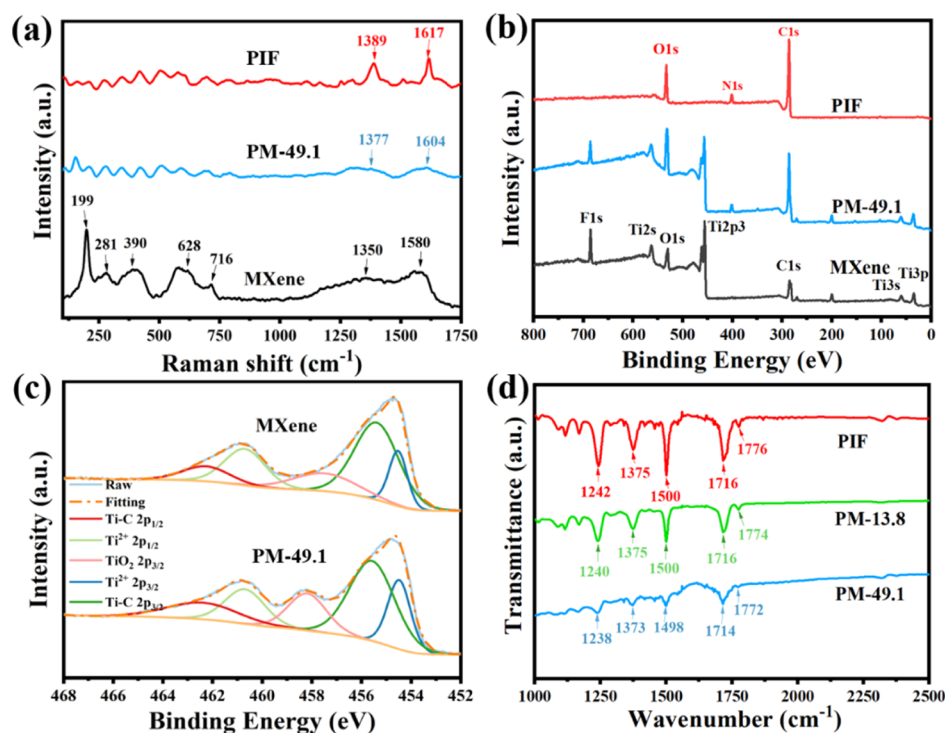


Figure 5. (a) Raman spectra, (b) XPS survey spectra, and (c) high-resolution Ti2p spectra of MXene and PM-49.1. (d) FTIR spectra of the pure PIF film, PM-13.8, and PM-49.1.

skeleton, and thermal-imidized PI serves as “cement” to weld-adjacent PIF and MXene-PIF strongly, ensuring the robustness of the prepared composite film. Such a special “rebar,” “brick,” and “cement” structure will undoubtedly be beneficial for excellent mechanical property and perfect conductive network of the prepared composite film.

Figure 4a shows the typical stress–strain curves of pure PIF and different PIF/MXene composite films. As expected, a significant enhancement in the mechanical property is clearly observed for the pure PIF film after thermal imidization treatment. Specially, as shown in Figure 4b and S6, tensile strength, Young’s modulus, and fracture elongation of the pure PIF film are increased from 3.56 to 5.13 MPa, 50.45 to 64.75 MPa, and 11.24 to 15.27%, respectively, which is mainly ascribed to the “cement” of thermal-imidized PI that effectively weld the loosely physically entangled PIF together, enabling it to bear stronger stress. As for the PIF/MXene composite film, tensile strength and Young’s modulus are further significantly improved to 21.72 and 527.43 MPa for PM-13.8, respectively. The large improvement in mechanical properties can be attributed to the special “rebar,” “brick” and “cement” structure, where the homogeneously dispersed MXene nanosheets in the PIF network and the strong PIF/MXene and PIF/PIF interfacial adhesion with the help of thermal-imidized PI can ensure the effective stress transfer inside the prepared composite film. With increasing MXene loading, Young’s modulus of the composite film displays an increasing trend, and a 1037% increase to 736.1 MPa is observed for PM-39.1. However, tensile strength and fracture elongation are obviously reduced. The reason can be explained by the fact that the agglomeration effect of MXene at higher loading leads to the weaker bonding effect of thermal-imidized PI. Besides, Young’s modulus also begins to decline for PM-49.1 due to an ultrahigh MXene loading. Figure 4c illustrates the electrical conductivity of different PIF/MXene

composite films before and after thermal imidization treatment. Obviously, benefiting from the dense PIF/MXene conductive network constructed by the thermal-imidized PI, an effective enhancement in electrical conductivities is achieved for all PIF/MXene composite films after the thermal imidization process. Meanwhile, higher MXene loading endows the composite film with higher electrical conductivity due to the construction of more perfect conductive network, and the electrical conductivity reaches 3787.9 S/m for PM-49.1 with a thickness of 132 μm . All these excellent mechanical property and electrical property stated above will undoubtedly enable the prepared conductive PIF/MXene composite film to be applicable for EMI shielding and Joule heating applications, which will be systematically investigated in the following part.

3.3. Raman, XPS, and FTIR Analysis. Raman, XPS, and FTIR were further conducted to study the chemical composition and interfacial interaction of the prepared PIF/MXene composite film. As for the Raman spectra shown in Figure 5a, the Raman peaks of MXene at 199 and 716 cm⁻¹ are ascribed to the A_{1g} symmetry out-of-plane vibrations of Ti and C atoms, respectively, and the peaks at 281, 390, and 628 cm⁻¹ are attributed to the E_g group vibrations, including in-plane shear modes of Ti, C, and surface functional group atoms.⁴⁶ The broad peaks at 1350 and 1580 cm⁻¹ correspond to the D and G bands of graphitic carbon of MXene, respectively.⁴⁷ Besides, the pure PIF film displays the typical C–N tensile vibration of the imide ring at 1389 cm⁻¹ and aromatic imide ring vibration of the dianhydride at 1617 cm⁻¹. As for the composite film of PM-49.1, all the typical peaks of PI and MXene overlap with each other, generating weaker and wider peaks at 1377 and 1604 cm⁻¹. All these can be ascribed to the charge transfer between MXene and PIF that leads to the average of the charge density between them, verifying the existence of good interfacial interactions. Figure 5b shows the XPS survey spectra of MXene, PIF, and PM-49.1.

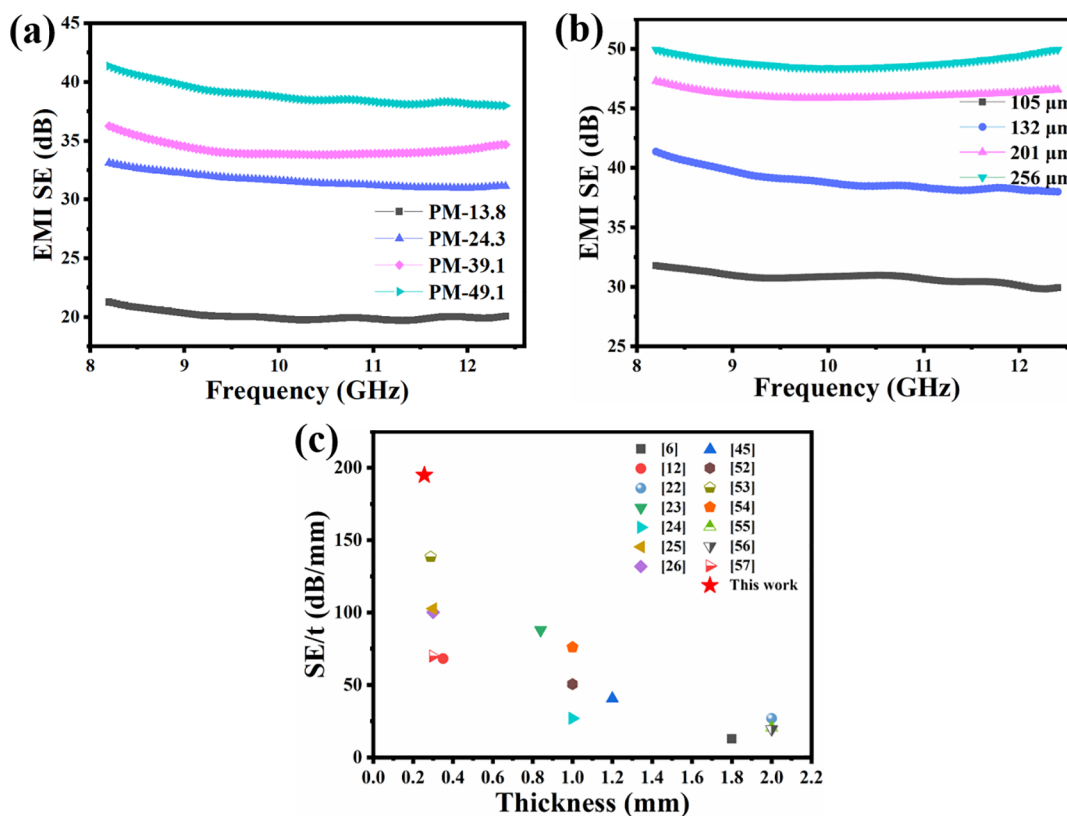


Figure 6. EMI SE of PIF/MXene composite films with (a) different MXene loadings and (b) different thicknesses in the frequency range of 8.2–12.4 GHz. (c) Comparison of SE/*t* of the PIF/MXene composite film with literature studies.

Clearly, all the representative elements of MXene (C, O, Ti, and F) and PIF (O, N and C) are observed for PM-49.1, indicating their successful combination. In addition, the high-resolution Ti2p spectra of MXene and PM-49.1 in Figure 5c illustrate that the TiO₂ percentage increases slightly from 12.49% for MXene to 15.52% for PM-49.1, which can be ascribed to the high-temperature oxidation of Ti during the thermal imidization process.³² However, it should be noted that the excellent oxygen barrier effect of thermal-imidized PI on MXene can effectively enhance the stability of MXene, enabling the composite film applicable in various harsh environments, which will be discussed in the following part. The FTIR spectra of PIF, PM-13.8, and PM-49.1 are shown in Figure 5d. The pure PIF film shows typical characteristic peaks of PI, including C–O stretching vibration at 1242 cm⁻¹, C–N stretching vibration at 1375 cm⁻¹, C=C stretching vibration in the benzene ring at 1500 cm⁻¹, and C=O symmetric and asymmetric stretching vibrations on the imine ring at 1716 and 1776 cm⁻¹. After mixing with MXene, it can be observed that most typical peaks of PI shift to a lower wavenumber, which can be due to the formation of a hydrogen bond between PI and MXene nanosheets, endowing it with excellent mechanical properties through effective stress transfer.⁴⁰

3.4. EMI Shielding Performance of PIF/MXene Composite Films. Figure 6a displays the EMI shielding performance of different conductive PIF/MXene composite films in the frequency range of 8.2–12.4 GHz. As expected, PM-13.8 presents a satisfactory EMI SE of about 20 dB, which meets the commercial-level EMI shielding applications. With increasing the MXene loading, the prepared PIF/MXene composite film shows an enhanced EMI shielding performance in the whole frequency range, and an average EMI SE value of 41.4 dB is

achieved for PM-49.1, indicating that about 99.99% incident microwave can be effectively shielded. Based on the classic Simon formula,⁴⁴ the enhanced EMI shielding performance is closely related to the improved electrical conductivity of the PIF/MXene composite film with higher MXene loading. Apart from electrical conductivity, the thickness of material also affects their actual EMI shielding performances. In this work, a series of PM-49.1 with different thicknesses were prepared from the materials and energy saving standpoint. As expected, thickness-dependent EMI shielding performances are observed from Figure 6b, where thicker PIF/MXene composite films present a higher EMI SE. Specifically, the average EMI SE values are calculated to be 31.8, 41.4, 47.3, and 49.9 dB for the sample with a thickness of 105, 132, 201, and 256 μm, respectively, which is enough to block 99.999% incident EMWs.

Then, the maximum EMI SE values achieved in this study and the values reported in the literatures are compared to highlight the excellent EMI shielding performance of the PIF/MXene composite film. Owing to the thickness-dependent EMI SE, the values of EMI SE normalized by the thickness (SE/*t*) are calculated to give a fair comparison. As shown in Table S1 and Figure 6c, our prepared PIF/MXene composite film possesses superior EMI shielding over other MXene-based composite materials and CPCs, which is mainly ascribed to the high electrical conductivity and the special “rebar,” “brick,” and “cement” lamellar structure. Herein, it can be concluded that our prepared flexible conductive PIF/MXene composite film is qualified to serve as highly efficient EMI shielding materials.

Generally, reflection and absorption are the two main shielding mechanisms toward EMW.^{48–51} In a conductive material, shielding by reflection (SE_R) can be expressed as:

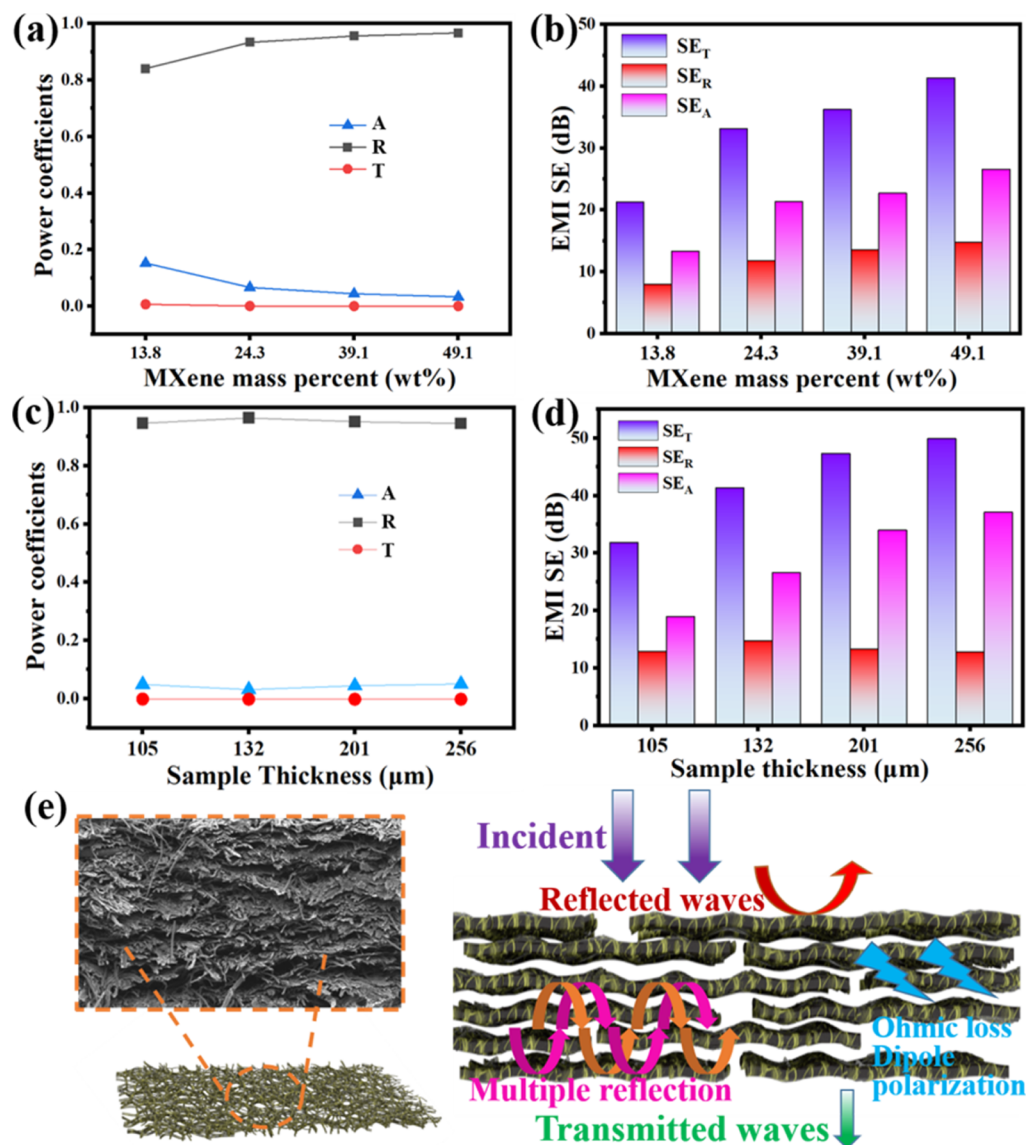


Figure 7. (a,c) Average power coefficients of A , R and T and (b,d) average SE_T , SE_R and SE_A of PIF/MXene composite films with different MXene loadings and different thicknesses in the frequency range of 8.2–12.4 GHz. (e) Schematic illustration showing the EMI shielding mechanism of the conductive PIF/MXene composite film.

$SE_R = 168 - 10 \cdot \log \frac{\mu_r^f}{\sigma_r}$, where f is frequency, μ_r is the permeability of the shielding material relative to that of free space, and σ_r is the conductivity of the shielding material relative to the conductivity of copper. Clearly, the shielding material with higher conductivity is beneficial for higher SE_R , while the existence of magnetic materials will lead to lower SE_R . As for the shielding by absorption (SE_A), EMW is mainly attenuated through the interaction with free-charge carriers and/or electric/magnetic dipoles. Generally, a shielding material with a thickness of l can be defined as: $SE_A = 131l\sqrt{f\mu_r\sigma_r}$. Hence, it be concluded that a material with higher conductivity and permeability possesses stronger EMW absorption efficiency. In addition, there is a linear relationship between shielding by absorption and thickness of a shield. As a matter of fact, the higher the thickness of a conductive shield, the greater is the amount of interacting free-charge carriers and/or electric/magnetic dipoles.^{52,53}

To further identify the EMI shielding mechanism of the conductive PIF/MXene composite film, the average power coefficients (A , R , and T) of PIF/MXene composite films with different MXene loadings are shown in Figure 7a. Clearly, R values are always higher than A values, indicating that most incident waves are attenuated by reflection due to the good interaction between the mobile charge carriers of shielding materials and electric vector of incident electromagnetic radiation. Herein, it can be concluded that the reflection is identified to be the dominant shielding mechanism of our prepared conductive PIF/MXene composite film. In addition, it can be found that increasing MXene loading gives rise to an increased reflectivity but decreased absorptivity, where the R value is up to 0.97 and the A value is only 0.03 for PM-49.1. Therefore, the reflection-dominated shielding mechanism can be effectively enhanced through increasing MXene loading. Figure 7b displays a comparison of average SE_T , SE_R , and SE_A of different conductive PIF/MXene composite films. Unlike the power coefficients analyzed above, SE_T , SE_R , and SE_A are

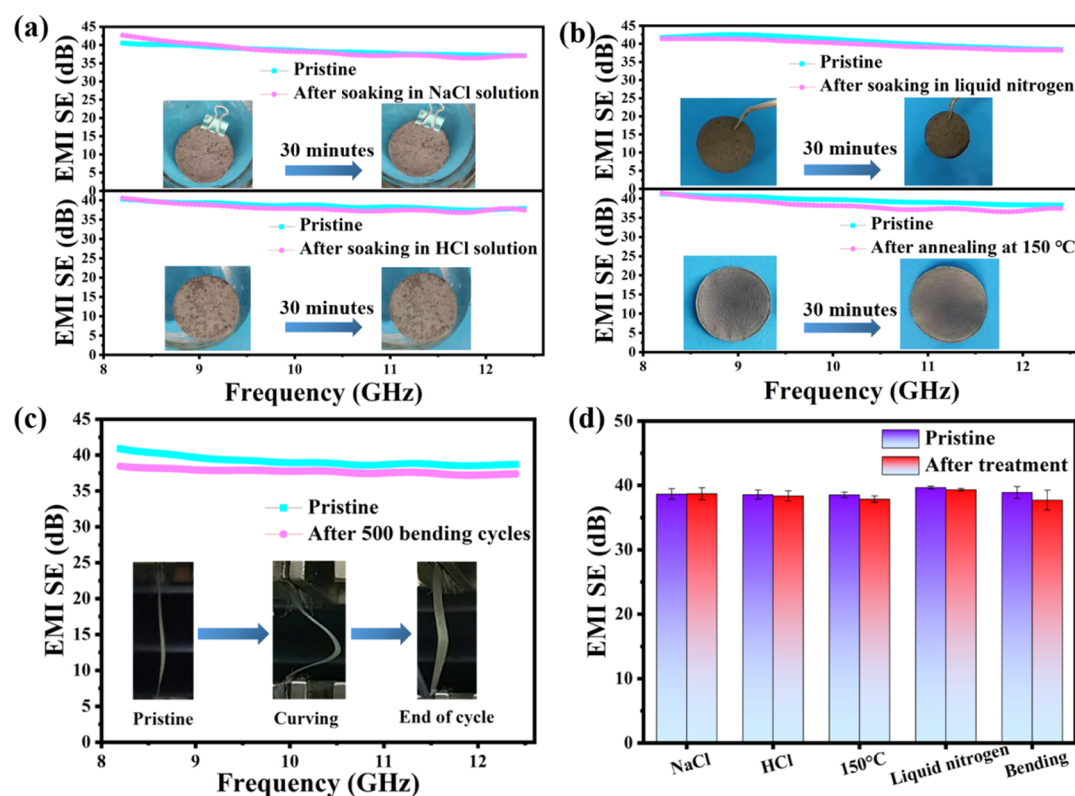


Figure 8. EMI shielding performances of the PM-49.1 before and after (a) soaking in NaCl/HCl solution, (b) soaking liquid nitrogen/annealing at 150 °C, and (c) repeated bending cycles. (d) Average SE_T before and after the treatment in different environments.

acquired based on the waves penetrating the material to exclude their reflected wave. Generally, absorption occurs before reflection for the incident waves, so SE_R and SE_A only represent the capability of shielding materials to attenuate the penetrated waves. Different from the power coefficients, both SE_A and SE_R increase with increasing MXene loading, and the contribution of SE_A to SE_T is up to >62.5% for all PIF/MXene composite films, making greater contribution than that of SE_R. Thus, the absorption mechanism plays a dominant role inside the materials, which will greatly avoid the secondary EMW pollution in practical applications. As for the thickness-dependent EMI shielding mechanism of PIF/MXene composite films, it can be clearly observed from Figure 7c that all the average power coefficients of different composite films are almost the same. Meanwhile, it should be noted from Figure 7d that the average SE_A increases with increasing thickness, but the average SE_R remains almost stable, demonstrating that the stronger EMI shielding performance of the thicker composite film stems from the enhanced absorption loss toward the incident waves.

As shown in Figure 7e, a schematic illustration showing the transmission process of EMW through the PIF/MXene composite film is proposed to get a better understanding of the shielding mechanism stated above. First, most EMWs are reflected immediately after injecting on the surface of the composite film, owing to the impedance mismatch between free air and shielding materials, which is mainly ascribed to the numerous free electrons at the MXene surface. Then, the incident EMW would be attenuated inside the materials through interacting with the high charge density MXene and generating electric conduction loss. Actually, the asymmetric distribution of charges at the interfaces between MXene and PIF, and the defects and terminal functional groups of MXene can also lead to

interfacial and dipolar polarization loss toward the incident EMW.³¹ Meanwhile, the special “rebar,” “brick,” and “cement” lamellar structure is also beneficial for the multiple reflection of EMW inside the materials to further enhance their EMW dissipation capacity. As a result, both the reflection and absorption of EMW contribute to an excellent EMI shielding performance.

3.5. EMI Shielding Performance of PIF/MXene Composite Films under Harsh Environments.

The flexible conductive PIF/MXene composite film was further treated in different environments to evaluate its EMI shielding stability, which is crucial for its practical applications. As shown in Figure 8a, PM-49.1 exhibits good structure integrity after being soaked into 0.5 mol/L NaCl solution and 0.5 mol/L HCl solution for 30 min, respectively. In addition, the EMI SE curve of the natural drying PM-49.1 after the soaking process almost coincided with that of the pristine sample, exhibiting stable EMI shielding performances. Similarly, as shown in Figure 8b and Video S1, PM-49.1 also exhibits good structure integrity, flexibility, and stable EMI shielding performances after being immersed in liquid nitrogen (−196 °C) and calcined at 150 °C for 30 min. All these can be ascribed to the good tolerance of PI to acid/salt and extreme temperature environments, where the good oxidation protection of MXene by PI ensures the stable electrical property of the composite film in the above special environments, resulting in such an excellent harsh environment tolerance.^{36–39}

Mechanical stability is also another important index to ensure the wider applicability of the PIF/MXene-based EMI shielding material. Obviously, as depicted in Figure 8c, the EMI shielding performance also remains almost unchanged after 500 bending cycles. Such a stable behavior can be ascribed to the special “rebar,” “brick,” and “cement” structure of PIF/MXene

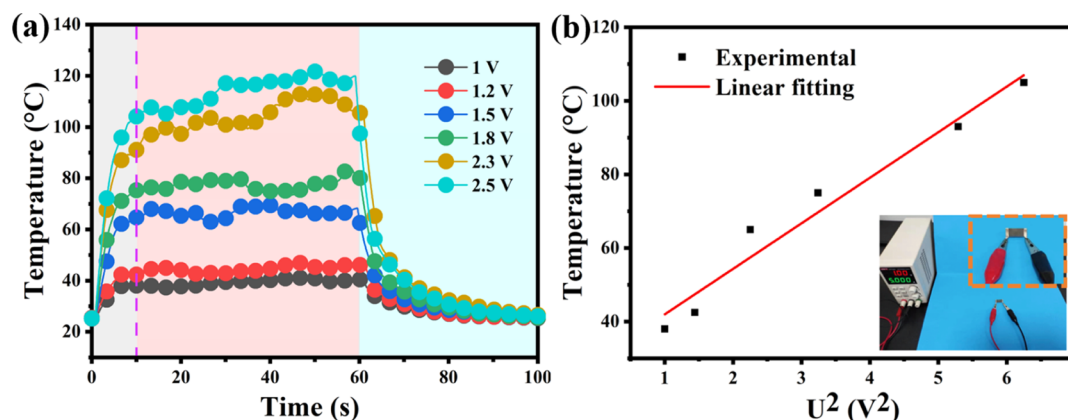


Figure 9. (a) Time-dependent surface temperature profile of PM-49.1 under different voltages. (b) Experimental data and linear fitting of saturated temperature vs U^2 .

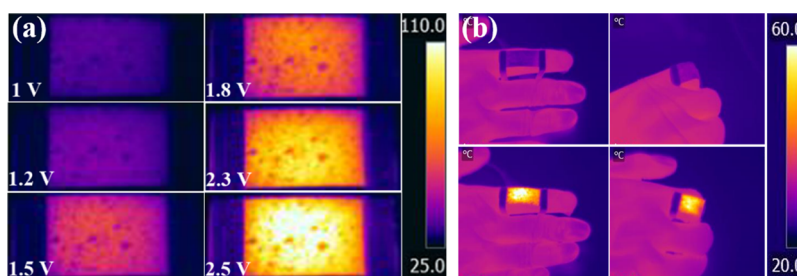


Figure 10. Infrared thermal images of PM-49.1 (a) at saturated temperature under different voltages and (b) applied to the bended finger under 1.5 V.

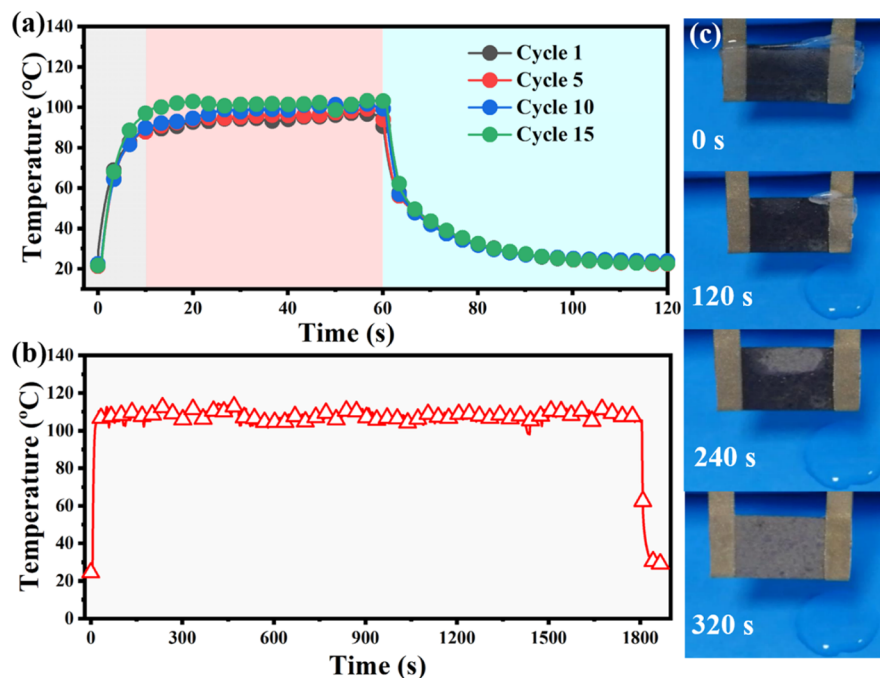


Figure 11. (a) Time-dependent surface temperature profiles of PM-49.1 in 1st, 5th, 10th, and 15th heating cycles under a voltage of 2.3 V. (b) Long-term temperature stability of PM-49.1 under a voltage of 2.3 V. (c) Optical images showing the thermal deicing performance of PM-49.1 under a voltage of 2.3 V.

composite films that endow it with excellent durability toward cyclic bending (Video S2). In addition, it can also be proved by the stable electrical property of the composite film during the cyclic bending process (Figure S7). Figure 8d comprehensively shows the comparison of the average EMI SE of the composite

film before and after being treated in different environments, and it can maintain stable EMI shielding performances with less than 3% degradation. Hence, it can be claimed that our prepared PIF/MXene composite film possesses wide application prospects in harsh external environments arising from the merits of PI,

including chemical resistance, thermal stability, high-/low-temperature resistance, and mechanical performance, which is usually impossible for the conventional polymer-based shielding materials.

3.6. Joule Heating Performance of PIF/MXene Composite Films. Based on Joule's law [$Q = (U^2/R)t$, Q is the generated heat in joule, U is the applied voltage, R is the resistance, and t is operating time], the good electrical conductivity of the prepared conductive PIF/MXene composite film can also endow it with excellent Joule heating performance, making it applicable for personal thermal management. Figure 9a shows the time-dependent temperature profile of PM-49.1 with a dimension of $1.75 \times 1.25 \text{ cm}^2$ recorded by an infrared thermal imaging camera under different voltages for 60 s and then cut off. Clearly, the surface temperature of PM-49.1 quickly rises from room temperature ($25.1 \text{ }^\circ\text{C}$) to a saturated temperature of 38, 42.5, 65, 75, 93, and $105 \text{ }^\circ\text{C}$ under a low voltage of 1, 1.2, 1.5, 1.8, 2.3, and 2.5 V within 10 s, respectively, indicating a fast thermal response and efficient electrothermal conversion. In addition, the applied low voltages that are far lower than the safe threshold of 36 V make it to be powered easily through a portable battery. Figure 9b shows the good linear relationship between the saturation temperature and the square of the voltage, which is well accorded with Joule's law, indicating a controllable Joule heating performance.

What is more, the uniform infrared thermal images at saturated temperature in Figure 10a present the homogeneous temperature distribution, which is critical for an ideal joule heater. In addition, the composite film can also be applied to personal thermal management under different human gestures, which can be verified by the simple application of human joint. When PM-49.1 is applied to the bended finger at a very low and safe voltage of 1.5 V, it exhibits stable and uniform electrothermal response during the bending process owing to the good flexibility and stable conductive network (Figure 10b).

To further explore the Joule heating performance of the prepared conductive PIF/MXene composite film in practical applications, cyclic and long-term electric heating tests were conducted for PM-49.1. As shown in Figure 11a, the time-dependent surface temperature profiles of PM-75 in 1st, 5th, 10th, and 15th heating cycles at a voltage of 2.3 V almost coincided with each other, showing the excellent reproductivity and recoverability. Meanwhile, the composite film also exhibits stable saturated temperature during a Joule heating process of 1800 s under a voltage of 2.3 V (Figure 11b), confirming the long-term durable Joule heating performance. Figure 11c and Video S3 show the application of the PIF/MXene composite film for thermal deicing and dehumidification in sub-zero temperature environments. As we can see clearly, both the front and back sides of the composite film are completely covered by ice, which is quickly melted and dripped after applying a voltage of 2.3 V for 120 s due to the Joule heating effect. After another 120 s, the moisture inside the composite film gradually evaporates, and the composite film turns to be completely dried in 320 s. In a conclusion, the excellent Joule heating property of the flexible conductive PIF/MXene composite film endows it with great applications in the thermal deicing of military aviation equipment and intelligent electronic equipment and the application of human thermal management.

4. CONCLUSIONS

In this work, flexible conductive PIF/MXene composite films with densely stacked "rebar-brick-cement" lamellar structure

were prepared using the simple vacuum-assisted filtration plus thermal imidization method. Here, the excellent flexibility of PIF and good binding effect of thermal-imidized PI solved the disadvantage of brittleness of the pure MXene film effectively, enabling it to be applicable in flexible wearable devices. When served as EMI shielding materials, the composite film exhibited the typical filler loading- and sample thickness-dependent shielding performances. Benefiting from the reflection and absorption of EMWs, the resultant PM-49.1 with a thickness of $256 \text{ }\mu\text{m}$ exhibited an EMI SE of 49.9 dB in the frequency range of 8.2–12.4 GHz. In addition, it also displays super Joule heating performances with fast response time, controllability, excellent cyclic stability, and good long-term durability. Impressively, the composite film displayed stable and durable EMI shielding performance toward harsh environments (e.g., extreme high-/low temperature, acid/salt solution, and long-term cyclic bending) and highly efficient thermal deicing performance under actual conditions. Therefore, our prepared flexible multifunctional composite film has great potential in EMW protection and personal thermal management.

■ ASSOCIATED CONTENT

Supporting Information

The Supporting Information is available free of charge at <https://pubs.acs.org/doi/10.1021/acsami.1c15467>.

Digital picture of the freeze-dried PIF; polarized optical microscopy showing that the average length of PIF is about $50 \text{ }\mu\text{m}$; digital photograph showing the brittleness of the pure MXene film; cross-sectional SEM images of PM-49.1; typical stress–strain curves and the corresponding mechanical properties of the pure PIF film before thermal imidization treatment; average power coefficients of A , R , and T of PM-49.1 with different thicknesses in the frequency range of 8.2–12.4 GHz; and resistance change curve of PM-24.3 and PM-49.1 during 500 bending cycles (PDF)

PM-49.1 exhibiting good structure integrity and flexibility after being immersed in liquid nitrogen ($-196 \text{ }^\circ\text{C}$) for 30 min (MP4)

PIF/MXene composite film exhibiting excellent durability toward cyclic bending (MP4)

Application of the PIF/MXene composite film for thermal deicing and dehumidification in sub-zero temperature environments (MP4)

■ AUTHOR INFORMATION

Corresponding Author

Hu Liu – Key Laboratory of Materials Processing and Mold (Zhengzhou University), Ministry of Education; National Engineering Research Center for Advanced Polymer Processing Technology, Zhengzhou University, Zhengzhou, Henan 450002, China; orcid.org/0000-0003-3840-8135; Email: liuhu@zzu.edu.cn

Authors

Kang Sun – Key Laboratory of Materials Processing and Mold (Zhengzhou University), Ministry of Education; National Engineering Research Center for Advanced Polymer Processing Technology, Zhengzhou University, Zhengzhou, Henan 450002, China

Fan Wang – Key Laboratory of Materials Processing and Mold (Zhengzhou University), Ministry of Education; National

Engineering Research Center for Advanced Polymer Processing Technology, Zhengzhou University, Zhengzhou, Henan 450002, China

Wenke Yang – Key Laboratory of Materials Processing and Mold (Zhengzhou University), Ministry of Education; National Engineering Research Center for Advanced Polymer Processing Technology, Zhengzhou University, Zhengzhou, Henan 450002, China

Caofeng Pan – Beijing Institute of Nanoenergy and Nanosystems; National Center for Nanoscience and Technology (NCNST), Chinese Academy of Sciences, Beijing 100083, China; orcid.org/0000-0001-6327-9692

Zhanhu Guo – Integrated Composites Laboratory (ICL), Department of Chemical & Biomolecular Engineering, University of Tennessee, Knoxville, Tennessee 37996, United States; orcid.org/0000-0003-0134-0210

Chuntai Liu – Key Laboratory of Materials Processing and Mold (Zhengzhou University), Ministry of Education; National Engineering Research Center for Advanced Polymer Processing Technology, Zhengzhou University, Zhengzhou, Henan 450002, China; orcid.org/0000-0001-9751-6270

Changyu Shen – Key Laboratory of Materials Processing and Mold (Zhengzhou University), Ministry of Education; National Engineering Research Center for Advanced Polymer Processing Technology, Zhengzhou University, Zhengzhou, Henan 450002, China

Complete contact information is available at:
<https://pubs.acs.org/10.1021/acsami.1c15467>

Notes

The authors declare no competing financial interest.

ACKNOWLEDGMENTS

The research was financially supported by the National Natural Science Foundation of China (51803191 and 12072325), the National Key R&D Program of China (2019YFA0706802), the 111 project (D18023), and the Key Scientific and Technological Project of Henan Province (202102210038).

REFERENCES

- (1) Bai, T.; Guo, Y.; Wang, D.; Liu, H.; Song, G.; Wang, Y.; Guo, Z.; Liu, C.; Shen, C. A resilient and lightweight bacterial cellulose-derived C/rGO aerogel-based electromagnetic wave absorber integrated with multiple functions. *J. Mater. Chem. A* **2021**, *9*, 5566–5577.
- (2) Shahzad, F.; Alhabeb, M.; Hatter, C. B.; Anasori, B.; Man Hong, S.; Koo, C. M.; Gogotsi, Y. Electromagnetic interference shielding with 2D transition metal carbides (MXenes). *Science* **2016**, *353*, 1137–1140.
- (3) Aakyir, M.; Yu, H.; Araby, S.; Ruoyu, W.; Michelmor, A.; Meng, Q.; Losic, D.; Choudhury, N. R.; Ma, J. Electrically and thermally conductive elastomer by using MXene nanosheets with interface modification. *Chem. Eng. J.* **2020**, *397*, 125439.
- (4) Yang, J.; Liao, X.; Wang, G.; Chen, J.; Tang, W.; Wang, T.; Li, G. Fabrication of lightweight and flexible silicon rubber foams with ultra-efficient electromagnetic interference shielding and adjustable low reflectivity. *J. Mater. Chem. C* **2020**, *8*, 147–157.
- (5) Lee, S. H.; Yu, S.; Shahzad, F.; Hong, J. P.; Kim, W. N.; Park, C.; Hong, S. M.; Koo, C. M. Highly anisotropic Cu oblate ellipsoids incorporated polymer composites with excellent performance for broadband electromagnetic interference shielding. *Compos. Sci. Technol.* **2017**, *144*, 57–62.
- (6) Gargama, H.; Thakur, A. K.; Chaturvedi, S. K. Polyvinylidene fluoride/nickel composite materials for charge storing, electromagnetic interference absorption, and shielding applications. *J. Appl. Phys.* **2015**, *117*, 224903.
- (7) Zhu, Y.; Liu, J.; Guo, T.; Wang, J. J.; Tang, X.; Nicolosi, V. Multifunctional Ti₃C₂T_x MXene Composite Hydrogels with Strain Sensitivity toward Absorption-Dominated Electromagnetic-Interference Shielding. *ACS Nano* **2021**, *15*, 1465–1474.
- (8) Wu, N.; Hu, Q.; Wei, R.; Mai, X.; Naik, N.; Pan, D.; Guo, Z.; Shi, Z. Review on the electromagnetic interference shielding properties of carbon based materials and their novel composites: Recent progress, challenges and prospects. *Carbon* **2021**, *176*, 88–105.
- (9) Ma, C.; Cao, W.-T.; Zhang, W.; Ma, M.-G.; Sun, W.-M.; Zhang, J.; Chen, F. Wearable, ultrathin and transparent bacterial celluloses/MXene film with Janus structure and excellent mechanical property for electromagnetic interference shielding. *Chem. Eng. J.* **2021**, *403*, 126438.
- (10) Yang, Y.; Feng, C.; Zhou, Y.; Zha, X.; Bao, R.; Ke, K.; Yang, M.; Tan, C.; Yang, W. Achieving improved electromagnetic interference shielding performance and balanced mechanical properties in polyketone nanocomposites via a composite MWCNTs carrier. *Composites, Part A* **2020**, *136*, 105967.
- (11) Cao, W. T.; Chen, F. F.; Zhu, Y. J.; Zhang, Y. G.; Jiang, Y. Y.; Ma, M. G.; Chen, F. Binary Strengthening and Toughening of MXene/Cellulose Nanofiber Composite Paper with Nacre-Inspired Structure and Superior Electromagnetic Interference Shielding Properties. *ACS Nano* **2018**, *12*, 4583–4593.
- (12) Kong, D.; Li, J.; Guo, A.; Xiao, X. High temperature electromagnetic shielding shape memory polymer composite. *Chem. Eng. J.* **2021**, *408*, 127365.
- (13) Wei, Q.; Pei, S.; Qian, X.; Liu, H.; Liu, Z.; Zhang, W.; Zhou, T.; Zhang, Z.; Zhang, X.; Cheng, H. M.; Ren, W. Superhigh Electromagnetic Interference Shielding of Ultrathin Aligned Pristine Graphene Nanosheets Film. *Adv. Mater.* **2020**, *32*, 1907411.
- (14) Liu, H.; Li, Q.; Bu, Y.; Zhang, N.; Wang, C.; Pan, C.; Mi, L.; Guo, Z.; Liu, C.; Shen, C. Stretchable conductive nonwoven fabrics with self-cleaning capability for tunable wearable strain sensor. *Nano Energy* **2019**, *66*, 104143.
- (15) Lin, S.; Wang, H.; Wu, F.; Wang, Q.; Bai, X.; Zu, D.; Song, J.; Wang, D.; Liu, Z.; Li, Z.; Tao, N.; Huang, K.; Lei, M.; Li, B.; Wu, H. Room-temperature production of silver-nanofiber film for large-area, transparent and flexible surface electromagnetic interference shielding. *npj Flexible Electron.* **2019**, *3*, 6.
- (16) Yin, R.; Yang, S.; Li, Q.; Zhang, S.; Liu, H.; Han, J.; Liu, C.; Shen, C. Flexible conductive Ag nanowire/cellulose nanofibril hybrid nanopaper for strain and temperature sensing applications. *Sci. Bull.* **2020**, *65*, 899–908.
- (17) Xie, F.; Jia, F.; Zhuo, L.; Lu, Z.; Si, L.; Huang, J.; Zhang, M.; Ma, Q. Ultrathin MXene/aramid nanofiber composite paper with excellent mechanical properties for efficient electromagnetic interference shielding. *Nanoscale* **2019**, *11*, 23382–23391.
- (18) Ma, Z.; Kang, S.; Ma, J.; Shao, L.; Zhang, Y.; Liu, C.; Wei, A.; Xiang, X.; Wei, L.; Gu, J. Ultraflexible and Mechanically Strong Double-Layered Aramid Nanofiber-Ti₃C₂T_x MXene/Silver Nanowire Nanocomposite Papers for High-Performance Electromagnetic Interference Shielding. *ACS Nano* **2020**, *14*, 8368–8382.
- (19) Guo, Y.; Zhong, M.; Fang, Z.; Wan, P.; Yu, G. A Wearable Transient Pressure Sensor Made with MXene Nanosheets for Sensitive Broad-Range Human-Machine Interfacing. *Nano Lett.* **2019**, *19*, 1143–1150.
- (20) Liu, J.; Liu, Z.; Zhang, H. B.; Chen, W.; Zhao, Z.; Wang, Q. W.; Yu, Z. Z. Ultrastrong and Highly Conductive MXene-Based Films for High-Performance Electromagnetic Interference Shielding. *Adv. Electron. Mater.* **2019**, *6*, 1901094.
- (21) Nepal, D.; Kennedy, W. J.; Pachter, R.; Vaia, R. A. Toward Architected Nanocomposites: MXenes and Beyond. *ACS Nano* **2021**, *15*, 21–28.
- (22) Sun, R.; Zhang, H.-B.; Liu, J.; Xie, X.; Yang, R.; Li, Y.; Hong, S.; Yu, Z.-Z. Highly Conductive Transition Metal Carbide/Carbonitride-(MXene)@polystyrene Nanocomposites Fabricated by Electrostatic Assembly for Highly Efficient Electromagnetic Interference Shielding. *Adv. Funct. Mater.* **2017**, *27*, 1702807.

- (23) Ghosh, S.; Nitin, B.; Remanan, S.; Bhattacharjee, Y.; Ghorai, A.; Dey, T.; Das, T. K.; Das, N. C. A Multifunctional Smart Textile Derived from Merino Wool/Nylon Polymer Nanocomposites as Next Generation Microwave Absorber and Soft Touch Sensor. *ACS Appl. Mater. Interfaces* **2020**, *12*, 17988–18001.
- (24) Nath, K.; Ghosh, S.; Ghosh, S. K.; Das, P.; Das, N. C. Facile preparation of light-weight biodegradable and electrically conductive polymer based nanocomposites for superior electromagnetic interference shielding effectiveness. *J. Appl. Polym. Sci.* **2021**, *138*, 50514.
- (25) Ghosh, S.; Mondal, S.; Ganguly, S.; Remanan, S.; Singha, N.; Das, N. C. Carbon Nanostructures Based Mechanically Robust Conducting Cotton Fabric for Improved Electromagnetic Interference Shielding. *Fibers Polym.* **2018**, *19*, 1064–1073.
- (26) Ghosh, S.; Das, P.; Ganguly, S.; Remanan, S.; Das, T. K.; Bhattacharyya, S. K.; Baral, J.; Das, A. K.; Laha, T.; Das, N. C. 3D-Enhanced, High-Performing, Super-hydrophobic and Electromagnetic-Interference Shielding Fabrics Based on Silver Paint and Their Use in Antibacterial Applications. *ChemistrySelect* **2019**, *4*, 11748–11754.
- (27) Zhang, H.; Zhang, G.; Gao, Q.; Tang, M.; Ma, Z.; Qin, J.; Wang, M.; Kim, J.-K. Multifunctional microcellular PVDF/Ni-chains composite foams with enhanced electromagnetic interference shielding and superior thermal insulation performance. *Chem. Eng. J.* **2020**, *379*, 122304.
- (28) Fang, H.; Wang, S.; Ye, W.; Chen, X.; Wang, X.; Xu, P.; Li, X.; Ding, Y. Simultaneous improvement of mechanical properties and electromagnetic interference shielding performance in eco-friendly polylactide composites via reactive blending and MWCNTs induced morphological optimization. *Composites, Part B* **2019**, *178*, 107452.
- (29) Zhou, B.; Zhang, Z.; Li, Y.; Han, G.; Feng, Y.; Wang, B.; Zhang, D.; Ma, J.; Liu, C. Flexible, Robust, and Multifunctional Electromagnetic Interference Shielding Film with Alternating Cellulose Nanofiber and MXene Layers. *ACS Appl. Mater. Interfaces* **2020**, *12*, 4895–4905.
- (30) Cao, W.; Ma, C.; Tan, S.; Ma, M.; Wan, P.; Chen, F. Ultrathin and Flexible CNTs/MXene/Cellulose Nanofibrils Composite Paper for Electromagnetic Interference Shielding. *Nano-Micro Lett.* **2019**, *11*, 72.
- (31) Iqbal, A.; Shahzad, F.; Hantanasirisakul, K.; Kim, M.-K.; Kwon, J.; Hong, J.; Kim, H.; Kim, D.; Gogotsi, Y.; Koo, C. M. Anomalous absorption of electromagnetic waves by 2D transition metal carbonitride Ti₃CNT_x (MXene). *Science* **2020**, *369*, 446–450.
- (32) Liu, J.; Zhang, H. B.; Xie, X.; Yang, R.; Liu, Z.; Liu, Y.; Yu, Z. Z. Multifunctional, Superelastic, and Lightweight MXene/Polyimide Aerogels. *Small* **2018**, *14*, 1802479.
- (33) Guo, Y.; Wang, D.; Bai, T.; Liu, H.; Zheng, Y.; Liu, C.; Shen, C. Electrostatic self-assembled NiFe₂O₄/Ti₃C₂T_x MXene nanocomposites for efficient electromagnetic wave absorption at ultralow loading level. *Adv. Compos. Hybrid Mater.* **2021**, *4*, 602–613.
- (34) Rajavel, K.; Yu, X.; Zhu, P.; Hu, Y.; Sun, R.; Wong, C. Exfoliation and Defect Control of Two-Dimensional Few-Layer MXene Ti₃C₂T_x for Electromagnetic Interference Shielding Coatings. *ACS Appl. Mater. Interfaces* **2020**, *12*, 49737–49747.
- (35) Lei, C.; Zhang, Y.; Liu, D.; Wu, K.; Fu, Q. Metal-Level Robust, Folding Endurance, and Highly Temperature-Stable MXene-Based Film with Engineered Aramid Nanofiber for Extreme-Condition Electromagnetic Interference Shielding Applications. *ACS Appl. Mater. Interfaces* **2020**, *12*, 26485–26495.
- (36) Guo, H.; Meador, M. A.; McCorkle, L.; Quade, D. J.; Guo, J.; Hamilton, B.; Cakmak, M.; Sprowl, G. Polyimide aerogels cross-linked through amine functionalized polyoligomeric silsesquioxane. *ACS Appl. Mater. Interfaces* **2011**, *3*, 546–552.
- (37) Pantoja, M.; Boynton, N.; Cavicchi, K. A.; Dosa, B.; Cashman, J. L.; Meador, M. A. B. Increased Flexibility in Polyimide Aerogels Using Aliphatic Spacers in the Polymer Backbone. *ACS Appl. Mater. Interfaces* **2019**, *11*, 9425–9437.
- (38) Zhu, Z.; Yao, H.; Dong, J.; Qian, Z.; Dong, W.; Long, D. High-mechanical-strength polyimide aerogels crosslinked with 4, 4'-oxydianiline-functionalized carbon nanotubes. *Carbon* **2019**, *144*, 24–31.
- (39) Nguyen, B. N.; Cudjoe, E.; Douglas, A.; Scheiman, D.; McCorkle, L.; Meador, M. A. B.; Rowan, S. J. Polyimide Cellulose Nanocrystal Composite Aerogels. *Macromolecules* **2016**, *49*, 1692–1703.
- (40) Liu, H.; Chen, X.; Zheng, Y.; Zhang, D.; Zhao, Y.; Wang, C.; Pan, C.; Liu, C.; Shen, C. Lightweight, Superelastic, and Hydrophobic Polyimide Nanofiber/MXene Composite Aerogel for Wearable Piezoresistive Sensor and Oil/Water Separation Applications. *Adv. Funct. Mater.* **2021**, *31*, 2008006.
- (41) Zheng, Y.; Yin, R.; Zhao, Y.; Liu, H.; Zhang, D.; Shi, X.; Zhang, B.; Liu, C.; Shen, C. Conductive MXene/cotton fabric based pressure sensor with both high sensitivity and wide sensing range for human motion detection and E-skin. *Chem. Eng. J.* **2021**, *420*, 127720.
- (42) Li, Q.; Yin, R.; Zhang, D.; Liu, H.; Chen, X.; Zheng, Y.; Guo, Z.; Liu, C.; Shen, C. Flexible conductive MXene/cellulose nanocrystal coated nonwoven fabrics for tunable wearable strain/pressure sensors. *J. Mater. Chem. A* **2020**, *8*, 21131–21141.
- (43) Bu, Y.; Shen, T.; Yang, W.; Yang, S.; Zhao, Y.; Liu, H.; Zheng, Y.; Liu, C.; Shen, C. Ultrasensitive strain sensor based on super-hydrophobic microcracked conductive Ti₃C₂T_x MXene/paper for human-motion monitoring and E-skin. *Sci. Bull.* **2021**, *66*, 1849–1857.
- (44) Chen, X.; Liu, H.; Zheng, Y.; Zhai, Y.; Liu, X.; Liu, C.; Mi, L.; Guo, Z.; Shen, C. Highly Compressible and Robust Polyimide/Carbon Nanotube Composite Aerogel for High-Performance Wearable Pressure Sensor. *ACS Appl. Mater. Interfaces* **2019**, *11*, 42594–42606.
- (45) Tang, X.-H.; Li, J.; Wang, Y.; Weng, Y.-X.; Wang, M. Controlling distribution of multi-walled carbon nanotube on surface area of Poly(ϵ -caprolactone) to form sandwiched structure for high-efficiency electromagnetic interference shielding. *Composites, Part B* **2020**, *196*, 108121.
- (46) Yan, J.; Ren, C. E.; Maleski, K.; Hatter, C. B.; Anasori, B.; Urbankowski, P.; Sarycheva, A.; Gogotsi, Y. Flexible MXene/Graphene Films for Ultrafast Supercapacitors with Outstanding Volumetric Capacitance. *Adv. Funct. Mater.* **2017**, *27*, 1701264.
- (47) Tong, Y.; He, M.; Zhou, Y.; Zhong, X.; Fan, L.; Huang, T.; Liao, Q.; Wang, Y. Electromagnetic wave absorption properties in the centimetre-band of Ti₃C₂T_x MXenes with diverse etching time. *J. Mater. Sci.: Mater. Electron.* **2018**, *29*, 8078–8088.
- (48) Shajari, S.; Arjmand, M.; Pawar, S. P.; Sundararaj, U.; Sudak, L. J. Synergistic effect of hybrid stainless steel fiber and carbon nanotube on mechanical properties and electromagnetic interference shielding of polypropylene nanocomposites. *Composites, Part B* **2019**, *165*, 662–670.
- (49) Chizari, K.; Arjmand, M.; Liu, Z.; Sundararaj, U.; Therriault, D. Three-dimensional printing of highly conductive polymer nanocomposites for EMI shielding applications. *Mater. Today Commun.* **2017**, *11*, 112–118.
- (50) Sharif, F.; Arjmand, M.; Moud, A. A.; Sundararaj, U.; Roberts, E. P. L. Segregated Hybrid Poly(methyl methacrylate)/Graphene/Magnetite Nanocomposites for Electromagnetic Interference Shielding. *ACS Appl. Mater. Interfaces* **2017**, *9*, 14171–14179.
- (51) Arjmand, M.; Chizari, K.; Krause, B.; Pötschke, P.; Sundararaj, U. Effect of synthesis catalyst on structure of nitrogen-doped carbon nanotubes and electrical conductivity and electromagnetic interference shielding of their polymeric nanocomposites. *Carbon* **2016**, *98*, 358–372.
- (52) Fan, Z.; Wang, D.; Yuan, Y.; Wang, Y.; Cheng, Z.; Liu, Y.; Xie, Z. A lightweight and conductive MXene/graphene hybrid foam for superior electromagnetic interference shielding. *Chem. Eng. J.* **2020**, *381*, 122696.
- (53) Raagulan, K.; Braveenth, R.; Lee, L. R.; Lee, J.; Kim, B. M.; Moon, J. J.; Lee, S. B.; Chai, K. Y. Fabrication of Flexible, Lightweight, Magnetic Mushroom Gills and Coral-Like MXene(-)Carbon Nanotube Nanocomposites for EMI Shielding Application. *Nanomaterials* **2019**, *9*, v519.
- (54) Han, M.; Yin, X.; Wu, H.; Hou, Z.; Song, C.; Li, X.; Zhang, L.; Cheng, L. Ti₃C₂ MXenes with Modified Surface for High-Performance Electromagnetic Absorption and Shielding in the X-Band. *ACS Appl. Mater. Interfaces* **2016**, *8*, 21011–21019.

(55) Wang, L.; Chen, L.; Song, P.; Liang, C.; Lu, Y.; Qiu, H.; Zhang, Y.; Kong, J.; Gu, J. Fabrication on the annealed Ti₃C₂T_x MXene/Epoxy nanocomposites for electromagnetic interference shielding application. *Composites, Part B* **2019**, *171*, 111–118.

(56) Liu, X.; Wu, J.; He, J.; Zhang, L. Electromagnetic interference shielding effectiveness of titanium carbide sheets. *Mater. Lett.* **2017**, *205*, 261–263.

(57) Xu, H.; Yin, X.; Li, X.; Li, M.; Liang, S.; Zhang, L.; Cheng, L. Lightweight Ti₂CT_x MXene/Poly(vinyl alcohol) Composite Foams for Electromagnetic Wave Shielding with Absorption-Dominated Feature. *ACS Appl. Mater. Interfaces* **2019**, *11*, 10198–10207.